Research Article

A low-firing melilite ceramic Ba$_2$CuGe$_2$O$_7$ and compositional modulation on microwave dielectric properties through Mg substitution

Changzhi YIN[a,c,†], Zezong YU[b,†], Longlong SHU[b],
Laijun LIU[c], Yan CHEN[a], Chunchun LI[a,b,c,*]

[a]*College of Information Science and Engineering, Guilin University of Technology, Guilin 541004, China*
[b]*School of Materials Science and Engineering, Nanchang University, Nanchang 330031, China*
[c]*Guangxi Universities Key Laboratory of Non-Ferrous Metal Oxide Electronic Functional Materials and Devices, College of Material Science and Engineering, Guilin University of Technology, Guilin 541004, China*

Abstract: A melilite Ba$_2$CuGe$_2$O$_7$ ceramic was characterized by low sintering temperature and moderate microwave dielectric properties. Sintered at 960 ℃, the Ba$_2$CuGe$_2$O$_7$ ceramic had a high relative density 97%, a low relative permittivity (ε_r) 9.43, a quality factor ($Q\times f$) of 20,000 GHz, and a temperature coefficient of resonance frequency (τ_f) –76 ppm/℃. To get a deep understanding of the relationship between composition, structure, and dielectric performances, magnesium substitution for copper in Ba$_2$CuGe$_2$O$_7$ was conducted. Influences of magnesium doping on the sintering behavior, crystal structure, and microwave dielectric properties were studied. Mg doping in Ba$_2$CuGe$_2$O$_7$ caused negligible changes in the macroscopic crystal structure, grain morphology, and size distribution, while induced visible variation in the local structure as revealed by Raman analysis. Microwave dielectric properties exhibit a remarkable dependence on composition. On increasing the magnesium content, the relative permittivity featured a continuous decrease, while both the quality factor and the temperature coefficient of resonance frequency increased monotonously. Such variations in dielectric performances were clarified in terms of the polarizability, packing fraction, and band valence theory.

Keywords: ceramics; dielectric properties; melilite structure; compositional modulation

1   Introduction

The development of wireless communication and broadband network technology has dramatically increased the demand for microwave dielectric materials, especially those being of small volume, low weight, high stability, and fast propagation speed [1,2]. The primary performance parameters that should be concerned are: (1) suitable relative permittivity ε_r depending on specific application scenarios, (2) high quality factors $Q\times f$ (or low dielectric loss), and (3) low-temperature drift of the resonance frequency (τ_f) [1–3]. Particularly, the official commercialization of the fifth-generation (5G) networks is expanding the operational frequency to microwave and millimeter

---

waves, and even terahertz bands [4,5]. To realize rapid signal propagation under so high frequencies, low relative permittivity is a prerequisite given that the decay for electromagnetic signal transmission in dielectric carriers is in proportion to the relative permittivity [6].

Up to now, there have been many studies on the exploration of low-ε_r dielectric materials, most of which highlight silicates such as $MgSiO_3$ (ε_r = 6.7), Zn_2SiO_4 (ε_r = 6.6), and $Ba_2ZnSi_2O_7$ (ε_r = 8.09) because of the low ionic polarizability of silicon (~0.87 Å^3) [7–9]. Among them, Si-based melilites with a chemical formula [$A_2BSi_2O_7$] have attracted intensive attention as microwave dielectric materials due to the ease with which the structures can accommodate different combinations of cations in the A and B sites [9–11]. The structure of $A_2BSi_2O_7$ melilite is represented as a two-dimensional framework of tetrahedral sheets of corner-sharing [SiO_4] and [BO_4] tetrahedra, in such a way that the [SiO_4] tetrahedra link at one corner to form [Si_2O_7] dimers and the four remaining corners in the dimer are linked to the [BO_4] tetrahedra. Consequently, a set of distorted pentagonal rings is formed and the big A ions enter these sites, providing the connection between adjacent sheets [12,13]. The compositional and structural flexibility of melilites provides wide space and potential for tunability in their physical properties. As regards, in our previous work, Ge substitution for Si was proposed to modify the sintering behavior and dielectric performance of $A_2BSi_2O_7$. Consequently, some Ge-based melilites $A_2BGe_2O_7$ (with A = Sr, Ba, and B = Zn, Mg) have been reported to possess encouraging microwave dielectric properties with ε_r = 7.76–9.0, $Q \times f$ = 13950–35700 GHz, and τ_f = (–84.4)–(–55) ppm/℃ [14,15].

Recent reports have featured that CuO, either as a low-melting-point (1086 ℃) ingredient or as a sintering aid, usually facilitates sintering and uprates dielectric behaviors [16,17]. For example, adding an appropriate amount of CuO in Mg_2SiO_4 stabilized the crystal structure and lowered the dielectric loss to some extent [18]. Wang *et al.* reported similar enhancement in sintering behavior and dielectric performances of $Li_3Mg_2NbO_6$ by CuO doping [19]. This inspires us to investigate melilites which would further yield a reduction in sintering temperature and improvement in dielectric properties.

Herein, $Ba_2CuGe_2O_7$, a member of melilites, was studied on the dielectric properties at microwave frequencies with an attempt to explore novel materials as potential candidates for microwave communication. Besides, given the identical valence and effective ionic radius for Mg^{2+} and Cu^{2+} in a tetra-coordinated group, the substituted magnesium in $Ba_2CuGe_2O_7$ is expected to induce certain structural variation on an either macroscopic or microscopic scale, which in turn engenders property evolutions. Doping effects on the sintering behavior, crystal structure, and microwave dielectric properties were studied.

2　Experimental

2.1　Material synthesis

A simple solid-state route was employed to fabricate $Ba_2Cu_{1-x}Mg_xGe_2O_7$ ceramics (x = 0, 0.2, 0.4, 0.6, and 0.8) using high-purity $BaCO_3$, CuO, GeO_2, and MgO (99.9%, Shanghai Aladdin, China) as raw materials, which were weighted according to the stoichiometry. Powder mixing via ball milling was conducted at a speed of 200 r/min for 4 h. After calcined at 900 ℃ for 4 h, the powders were secondly milled for particle uniformity, after which an appropriate amount of polyvinyl alcohol binder (5 wt%) was added. Then green pellets were pressed into cylinders with a diameter of 12 mm and 6 mm of thickness under a uniaxial pressure of 100 MPa. All green pellets firstly sintered at 550 ℃ with a heating rate 1.5 ℃/min for 6 h to remove the organic binder. And then, sintering behavior was performed in a temperature range from 900 to 1140 ℃ to achieve the best density, which was measured based on the Archimedes method.

2.2　Characterizations

The phase formation and purity were determined by X-ray diffraction using a Bruker Corporation diffractometer (D8 ADVANCE03030502, Karlsruhe, Germany). The Rietveld parameters of the scale factor, zero shift, unit cell parameters, background polynomial, profile parameters, atomic positional coordinates, and isothermal factors were refined step-by-step to improve the value of reliability factors. The microstructures were performed on the polished and thermal etched surfaces of the $Ba_2CuGe_2O_7$ (BCG) ceramics and measured by a scanning electron microscope (JSM-6701 F, Akishima City, Japan). Before SEM measurements, gold sputtering was done using a sputter coater (Ted Pella, USA). Micro Raman Spectroscopy System (Witec,

Ulm, Germany) is used for obtaining the Raman spectra with an argon ion laser (λ = 514.5 nm) as the excitation light. Raman shifts were measured with a precision of ~0.3 cm^{-1}. The spectral resolution is of the 1 cm^{-1} order and the range of it is 150–1200 cm^{-1}. Microwave dielectric properties were measured by a Vector Network Analyzer (Rohde & Schwarz, Munich, Germany). According to the Hakki–Coleman method, the relative permittivity (ε_r) and quality factor ($Q \times f$) were measured in the frequency range 10–16 GHz with a TE011 resonant mode. The temperature coefficient of resonance frequency (τ_f) was determined by recording the frequency drift over a temperature range from 25 to 85 ℃ in a temperature cavity and calculated based on the equation:

$$\tau_f = \frac{f_2 - f_1}{f_1(T_2 - T_1)} \tag{1}$$

3 Results and discussion

3.1 Crystal structure and dielectric properties of Ba$_2$CuGe$_2$O$_7$

Figure 1 shows the room-temperature XRD pattern and the calculated profile based on the Rietveld refinement performed on the Ba$_2$CuGe$_2$O$_7$ ceramic sintered at 960 ℃ for 6 h. A tetragonal melilite structure model with space group P-42$_1$$m$ (113) was adopted for refinement. The calculated pattern fits well with the
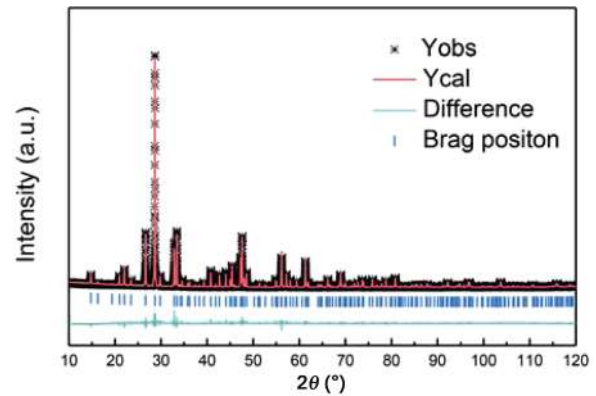

Fig. 1 Room-temperature XRD pattern and Rietveld refinement plots for Ba$_2$CuGe$_2$O$_7$.

observed one, yielding low reliable factors with R_p = 6.02% and R_{wp} = 7.73%. This result confirms the phase purity and the crystal structure of Ba$_2$CuGe$_2$O$_7$. The refined lattice parameters are a = b = 8.5133 Å, c = 5.4495 Å, and V = 390.2468 Å^3.

To explore the sintering behavior of Ba$_2$CuGe$_2$O$_7$ ceramics, the microstructure evolution and density variation as a function of sintering temperature was recorded and shown in Fig. 2. Evident grain growth was detected accompanied by a decrease in porosity as the sintering temperature increased, both signatures for densification. Consequently, a dense microstructure with grains about 5–7 μm was obtained after sintered at 960 ℃ (Fig. 2(d)). Correspondingly, the density (Fig. 2(f)) experienced an obvious increase from 4.65 g/cm^3 (~92% theoretical density) at 900 ℃ to 4.93 g/cm^3 (~97%) at 960 ℃. The slight decrease in density
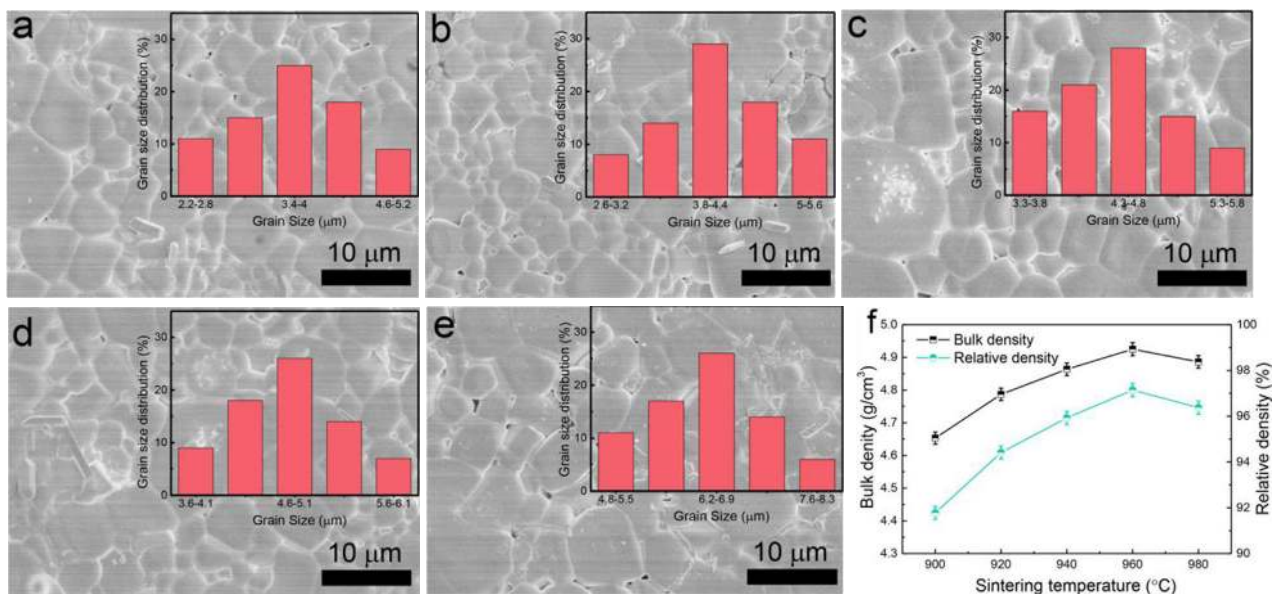

Fig. 2 SEM micrographs of the polished and thermal etched surfaces of the Ba$_2$CuGe$_2$O$_7$ ceramics sintered at (a) 900 ℃, (b) 920 ℃, (c) 940 ℃, (d) 960 ℃, and (e) 980 ℃; (f) the bulk density and relative density as a function of sintering temperature.

(4.89 g/cm^3) when sintered at 980 ℃ might be related to the large grains that give rise to re-entrant pores, as shown in Fig. 2(e).

Figure 3 shows the variations in the dielectric properties (ε_r, $Q\times f$, and τ_f) of the Ba$_2$CuGe$_2$O$_7$ ceramics sintered at a temperature range from 900 to 980 ℃. As the sintering temperature increased both ε_r and $Q\times f$ revealed a similar change trend resembling the density (Fig. 2(f)). A saturated value of $\varepsilon_r \approx 9.43$ and $Q\times f \approx 20{,}000$ GHz was obtained in the sample sintered at 960 ℃. It is well known that synergetic contributions from the extrinsic and intrinsic factors engender the overall variation in dielectric performances [20–22]. Herein, the strong correlation of the relative permittivity and quality factor on the density reveals a predominant role of density on the dielectric properties of Ba$_2$CuGe$_2$O$_7$. By contrast, the τ_f was weakly dependent on the sintering temperature and fluctuated around −76 ppm/℃. In summary, a composition sintered at 960 ℃ possessed the optimal microwave dielectric properties with $\varepsilon_r = 9.43$, $Q\times f = 20{,}000$ GHz, and $\tau_f =$ −76 ppm/℃.

The lower densification temperature of Ba$_2$CuGe$_2$O$_7$ ceramic than the melting point of the Ag electrode suggests that it has a promising application prospect in LTCC technology. Figure 4 shows XRD patterns, backscattering micrograph (BSEM), and EDS profile of the cofired Ba$_2$CuGe$_2$O$_7$ ceramic with the silver electrode at 960 ℃. By elaborate comparison with the
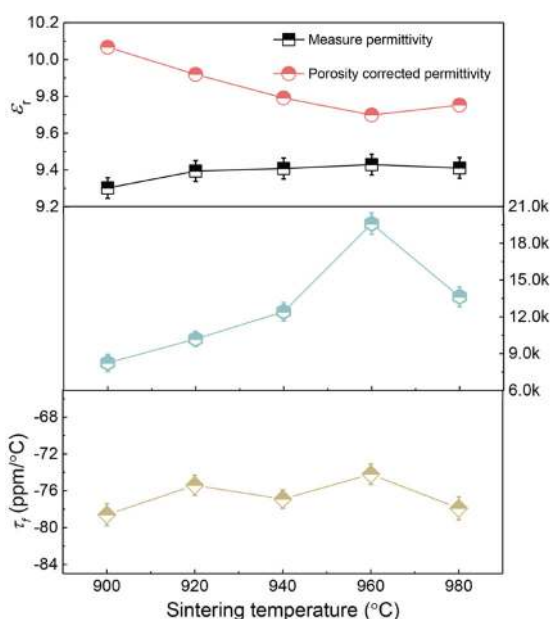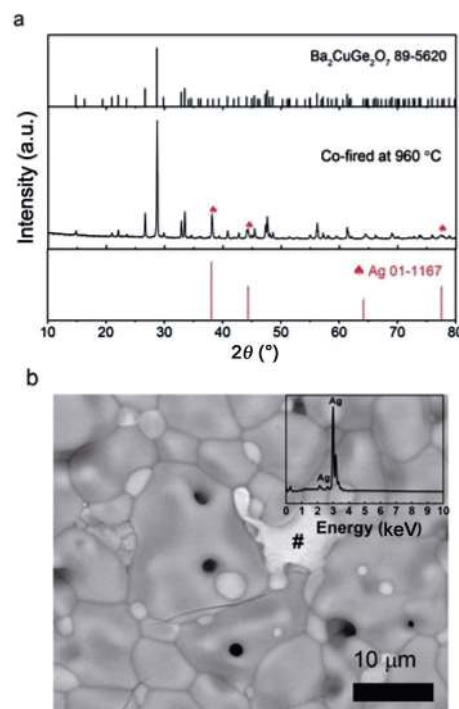

Fig. 4 (a) XRD and (b) SEM micrograph of Ba$_2$CuGe$_2$O$_7$ ceramic cofired with Ag electrode at 960 ℃ (EDS analysis of Ag is shown in the inset of Fig. 4(b)).

standard JCPDF cards, the diffraction peaks of silver are separated from those of the melilite. Two kinds of grains with different morphologies and element contrasts (bright grains and dark grains) can be detected. Combined with the EDS analysis, the bright grains are confirmed to be the Ag electrode.

By comparison with Ba$_2$MgGe$_2$O$_7$ ($\varepsilon_r = 7.76$, $Q\times f = 20{,}700$ GHz, and $\tau_f = −55$ ppm/℃), the present Cu-based compound has a higher relative permittivity, while its quality factor and the thermal stability of resonance frequency are inferior to those of Ba$_2$MgGe$_2$O$_7$ [14]. Thus, Mg substitution for Cu in Ba$_2$CuGe$_2$O$_7$ was conducted with an attempt to tune the dielectric performances of Ba$_2$CuGe$_2$O$_7$ and to correlate such dielectric evolutions to the composition and crystal structure.

3. 2 Effects of magnesium substitution on crystal structure and microstructure

The equivalent substitution of Mg for Cu caused no change in the macroscopic crystal structure of melilite Ba$_2$CuGe$_2$O$_7$ but indeed induced continuous variation in lattice parameters. Figure 5(a) shows XRD patterns recorded on the calcined Ba$_2$Cu$_{1-x}$Mg$_x$Ge$_2$O$_7$ ($x = 0$, 0.2, 0.4, 0.6, and 0.8) powders at 900 ℃. A similar pattern
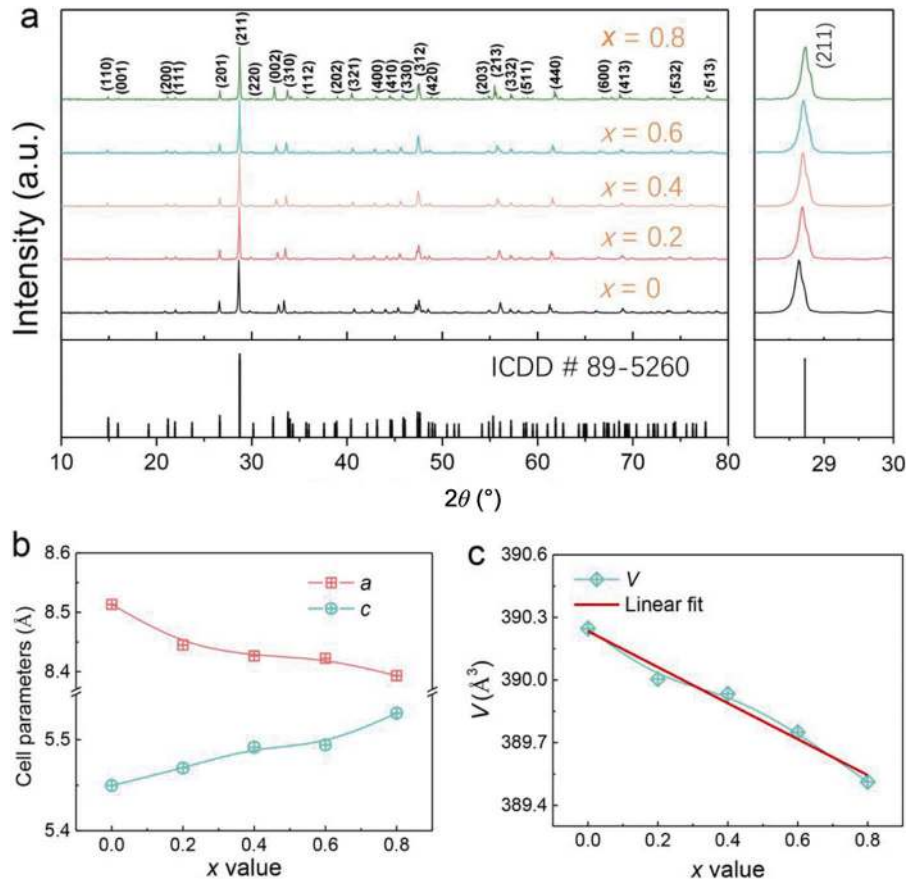

Fig. 3 Microwave dielectric properties of Ba$_2$CuGe$_2$O$_7$ ceramics sintered at different temperatures (900–980 ℃).

Fig. 5 (a) Room-temperature XRD patterns for $Ba_2Cu_{1-x}Mg_xGe_2O_7$ (x =0, 0.2, 0.4, 0.6, and 0.8) powders calcined at 900 ℃; (b, c) variations in the lattice parameters as a function of composition x.

is observed for all compositions and by indexing with ICDD # 89-5260 for $Ba_2CuGe_2O_7$, all peaks can be assigned and no additional peak is detected. The compositional-induced shift of (211) peak to the higher angle provides evidence of magnesium solution, despite the shift is not sizeable. The lattice parameters refined by the least-square method are obtained from Rietveld refinements. As presented in Fig. 5(b), an evident decrease in a is accompanied by a continuous increase in c, giving rise to a slight and monotonous decline in the unit cell by 0.18%. Otherwise, the linear variation in lattice parameters validates the Vegard's law for a solid solution. These results indicate the scheduled magnesium could completely dissolve into the lattice of melilite to form an infinite solid solution.

Rietveld refinements, shown in Fig. 6, further verifying the phase purity and structural stability, are characterized by the good match between the calculated and experimental profiles and the reliable residual factors. It should be noted that the structural model was established based on the parent $Ba_2CuGe_2O_7$ and the sequences for refinements were set as scale factor, zero shift, background, lattice parameters, peak function parameters, and atomic positions, etc. Importantly, the atomic position for magnesium was fixed in the Cu positions and their distribution was set as random.

Figures 7(a) and 7(b) illustrate the variation in bulk density as a function of sintering temperature and composition. All compositions exhibit an analogous dependence on sintering temperature of the density. An initial substantial increase in bulk density explains the crucial role of sintering temperature in promoting densification. A maximum bulk density (ρ_m) was achieved at a characteristic temperature (recognized as the optimized temperature, T_m) depending on composition. The compositional dependence of the ρ_m and T_m values is shown in Fig. 7(b), from which we can see that all compositions have a high relative density (> 96%), suggesting they are applicable for subsequent dielectric characterizations. The much higher melting point of MgO (2852 ℃) than that of CuO (1026 ℃) accounts for the increase in sintering behavior.

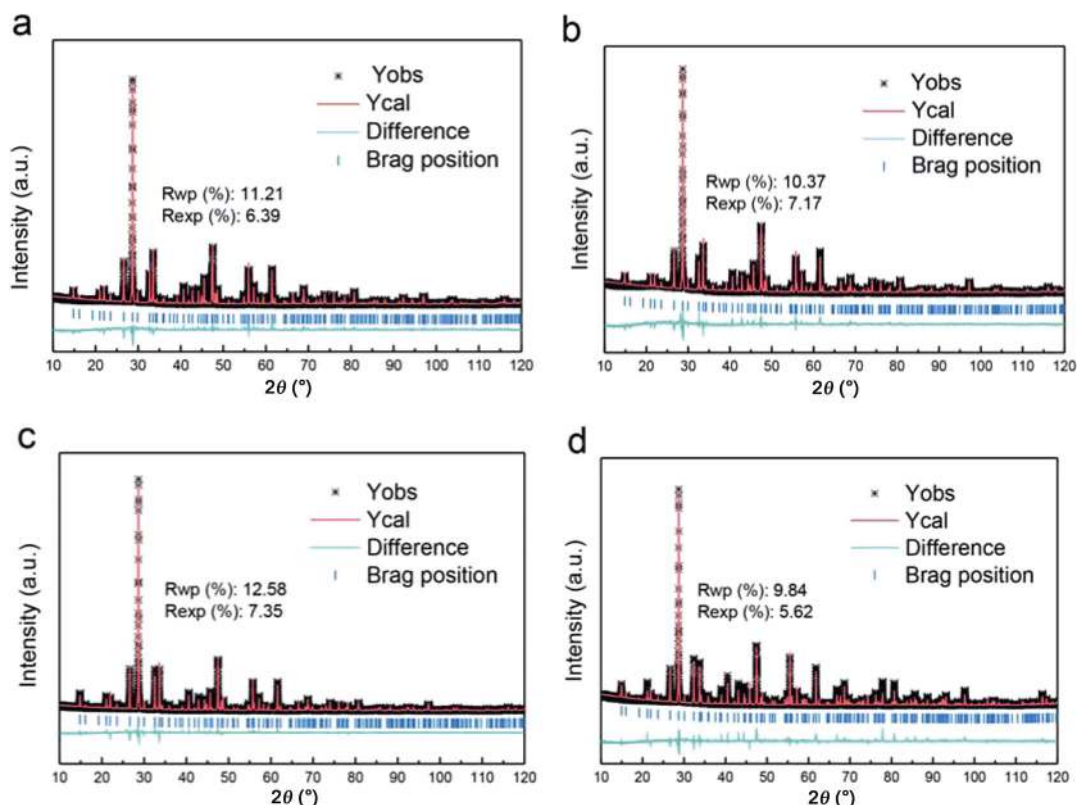Figures 8(a)–8(e) show SEM images of the polished

Fig. 6 Rietveld refinement plots for $Ba_2Cu_{1-x}Mg_xGe_2O_7$: (a) $x = 0.2$; (b) $x = 0.4$; (c) $x = 0.6$; (d) $x = 0.8$.
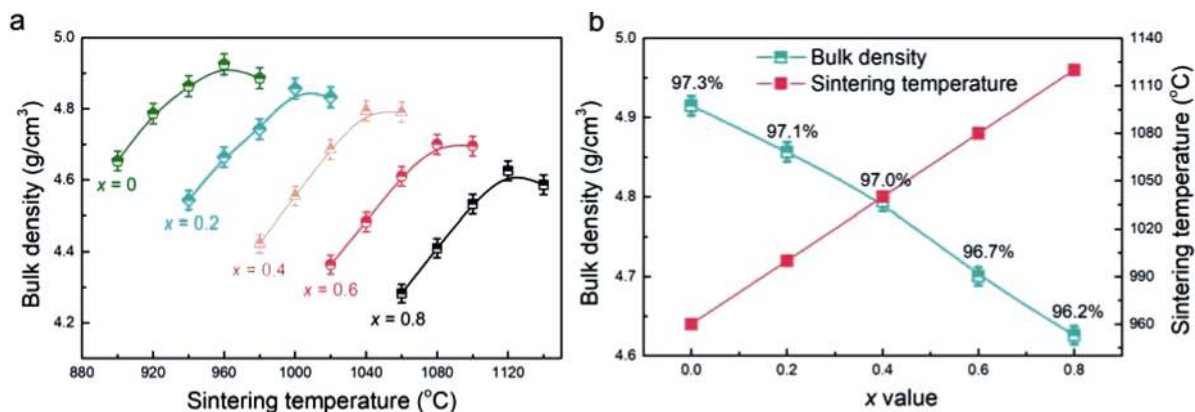

Fig. 7 (a) Variations in bulk density as a function of sintering temperature for $Ba_2Cu_{1-x}Mg_xGe_2O_7$; (b) compositional dependence of bulk density and sintering temperature with the relative densities showing in the inset.

and thermal etched surfaces of Mg-doped BCG along with their respective grain size distribution. Dense microstructures with few pores were developed for each compound, coincident with their high relative density. The similar grain morphology validated no structural transformation by Mg doping, which coincides with the XRD observation. Besides, the grain size distribution (in the inset of Fig. 8) for all compounds is alike, giving rise to their close average grain size, as shown in Fig. 8(f).

Table 1 Wyckoff sites for atoms and the corresponding Raman active modes in $Ba_2Cu_{1-x}Mg_xGe_2O_7$

Atom	Wyckoff site	Raman active modes
Ba	4e	$2A_1+B_1+2B_2+3E$
Cu (or Mg)	2a	B_1+B_2+2E
Ge	4e	$2A_1+B_1+2B_2+3E$
O	8f	$3A_1+3B_1+3B_2+6E$
2O	4e	$2A_1+B_1+2B_2+3E$
3O	2c	A_1+B_2+2E

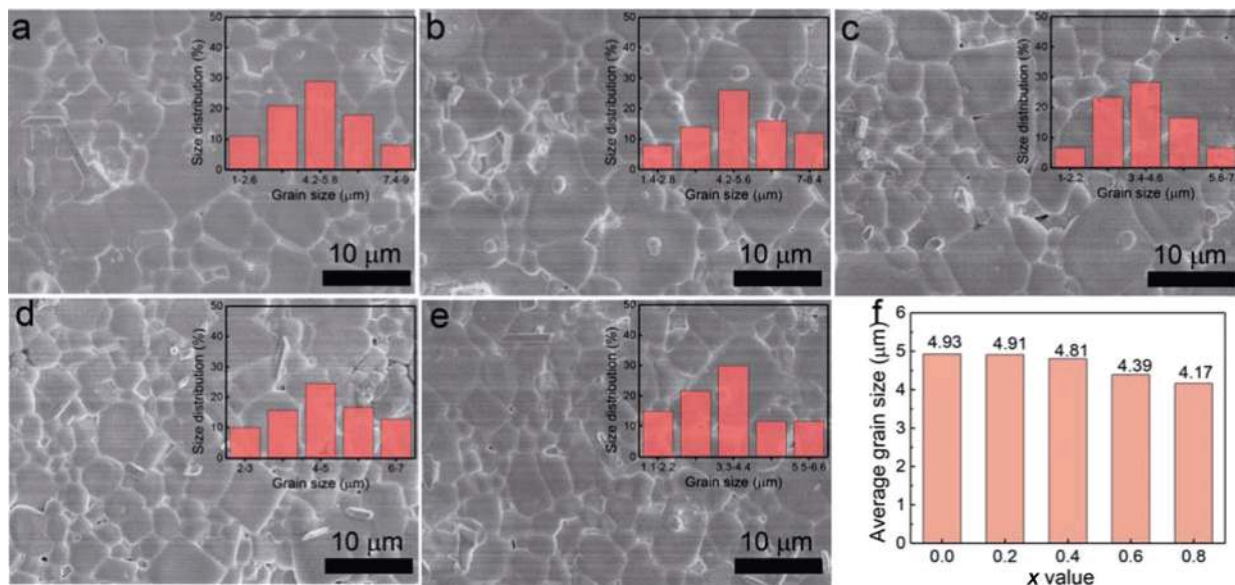**Fig. 8** (a–e) SEM images and the grain size distributions for $Ba_2Cu_{1-x}Mg_xGe_2O_7$ sintered at their optimum temperature; (f) the change of average grain size as a function of x value.
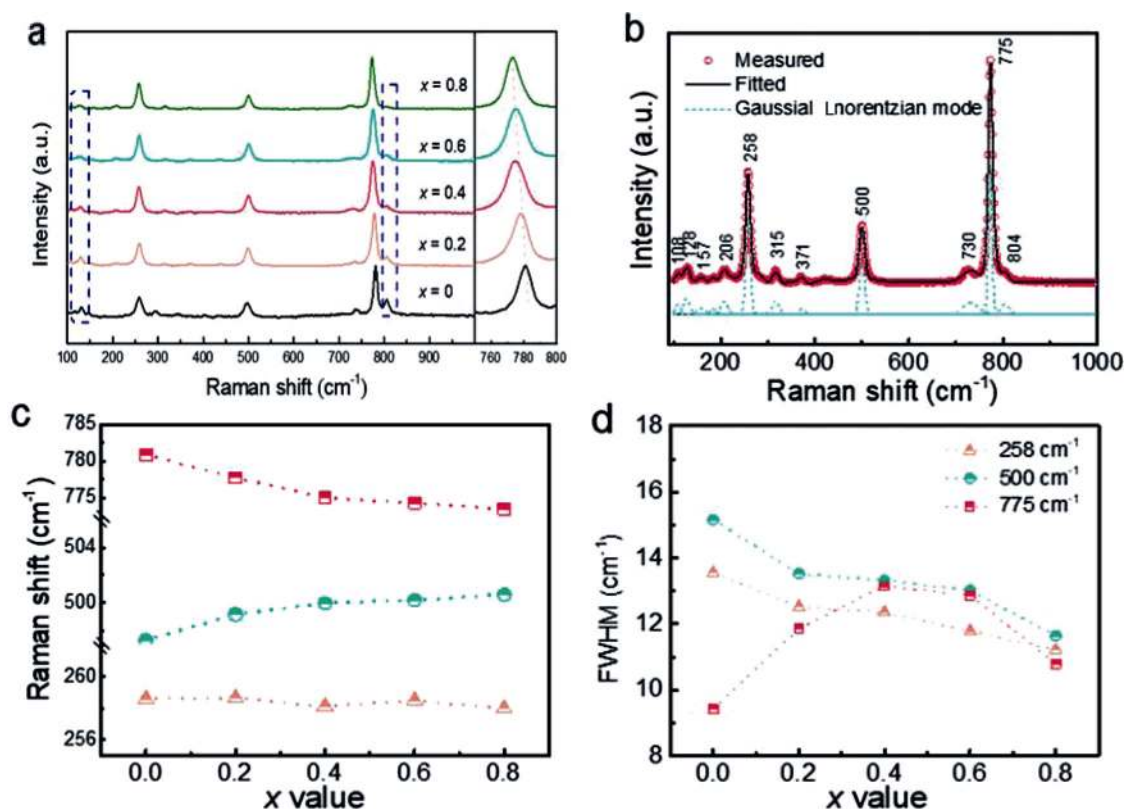

Fig. 9 (a) Raman spectroscopies for $Ba_2Cu_{1-x}Mg_xGe_2O_7$ along with an enlarged profile around 775 cm^{-1}; (b) a representative deconvolution fitting for the $x = 0.8$ composition; (c, d) variations in the Raman shift and FWHM for the three strongest Raman modes at 775 cm^{-1}, 500 cm^{-1}, and 258 cm^{-1}.

Raman scattering is known to be highly sensitive to the local structure variations, especially those induced by composition [12,23]. For a tetragonal $P\text{-}42_1m$ unit cell in $Ba_2CuGe_2O_7$, theoretically, the Raman active vibration modes are predicted based on the factor group theory and listed in Table 1 along with the Wyckoff sites. A total number of 45 ($\Gamma = 10A_1 + 7B_1 + 10B_2 + 18E$) Raman active modes are estimated.

Figure 9(a) shows the room-temperature Raman spectra of the $Ba_2Cu_{1-x}Mg_xGe_2O_7$ samples. Due to the low density and overlapping of some modes, only a limited number of Raman modes (11–16) are observed via the Gauss–Lorenzian deconvolution (Fig. 9(b)), among which the three strongest peaks appear around 775 cm^{-1}, 500 cm^{-1}, and 258 cm^{-1}, respectively. As well known, the Raman spectroscopy includes the internal vibrations of the framed polyhedron (either tetrahedron or octahedron for oxides) and the external ones from translational and liberational moves [23]. Generally, the binding energy in the polyhedral is larger than the intergroup or crystal energy, and thus the internal Raman modes usually appear at high-frequency bands. Thus, the strongest peak around 775 cm^{-1} is assigned as the symmetric stretching vibration of $[GeO_4]$, and the Raman mode around 500 cm^{-1} and 258 cm^{-1} corresponds to the asymmetric and symmetric bending of $[GeO_4]$, respectively. Nevertheless, the Raman modes related to the translation of Cu^{2+}/Mg^{2+} locate around 200–225 cm^{-1} and 280–300 cm^{-1}, as previously reported [12]. It should be noted that in the structure of melilite $Ba_2CuGe_2O_7$, the $[CuO_4]$ tetrahedra are corner-linked to the $[Ge_2O_7]$ dimers. Thus, the variation in the $[CuO_4]$ tetrahedra by Mg doping, either distortion/titling or volume expansion/shrinkage would cause a corresponding change in the neighboring $[GeO_4]$ tetrahedra. Hence, by recording the alteration in the $[GeO_4]$ tetrahedra, the local structure evolution by Mg substitution can be manifested.

The change of Raman shift and the full width at half maximum (FWHM) of the strongest three modes are shown in Figs. 9(c) and 9(d). As shown, the 775 cm^{-1} mode is markedly red-shifted, while the 500 cm^{-1} and 258 cm^{-1} modes are quasi-invariant with increasing composition x. The red-shift in the 775 cm^{-1} mode indicates the decreased band energy of the $[GeO_4]$ tetrahedra. This can be explained by the increased bond length of Ge–O caused by the expansion in the $[GeO_4]$ because of the compress of the adjacent $[Cu/MgO_4]$ tetrahedra. On the other hand, the width of the 500 cm^{-1} and 258 cm^{-1} modes monotonously decreased with increasing Mg content, while the 775 cm^{-1} mode was firstly broadened and then narrowed, resulting in the $x = 0.4$ composition featuring the highest FWHM. These results revealed that magnesium substitution induced local disorder, which becomes more distinct around $x = 0.4$.

More importantly, an extra mode in the parent $Ba_2CuGe_2O_7$ phase arises at 804 cm^{-1} and its intensity becomes weaker on the increasing magnesium content. This mode is assigned as the asymmetric stretching vibration of $[GeO_4]$. By comparing the Raman modes for $Ba_2MgGe_2O_7$ and $Ba_2ZnGe_2O_7$, a pretty evident difference lies in the absence or presence of this 804 cm^{-1} mode. In consideration of their same structure and atomic distribution, this distinction in Raman spectroscopy is believed to be related to the local structure distortion by Zn replacement for Mg. Similar phenomenon observed in this work validates the influences of magnesium substitution on the local structure.

In summary, magnesium substitution in $Ba_2CuGe_2O_7$ does not cause macroscopic phase transformation, or induce the second phase, or change the grain morphology and grain size distribution, but the evolutions in XRD peaks and Raman modes reveal that such doping indeed arouses local structural distortion, which could exert significant influences on dielectric properties.

3. 3   Effects of magnesium substitution on dielectric properties

Figures 10(a) and 10(b) represent the change of relative permittivity (ε_r) and quality factor ($Q \times f$) as a function of sintering temperature. For each composition, both ε_r and $Q \times f$ value increased as the sintering temperature increased and then decreased slightly. Importantly, the variation tendency of ε_r and $Q \times f$ versus sintering temperature is similar to that of density, being an indicator for the crucial role of density on dielectric performances. Generally, the highest ε_r and $Q \times f$ values for each position are achieved in the densest sample. Figures 10(c) and 10(d) summarize the optimum ε_r and $Q \times f$ values for various compositions. Strong dependence on composition is visible for both quantities. Relative permittivity features a noticeable decrement with increasing Mg content from 9.05 at $x = 0$ to 7.92 at $x = 0.8$. Conversely, the quality factor exhibits a continuous rise from 20,000 to 31,370 GHz as the amount of Mg increased from 0 to 0.8.

As well known, the relative permittivity and losses at microwave frequency bands not only depend on the intrinsic factors, but also the extrinsic ones from density (or pore), grain size, phase constitution, and phase transition, etc. [20,24–26]. Evidenced from the crystal structure and microstructure, magnesium substitution did not cause phase transformation, or induce the second phase, or change the grain morphology and grain size
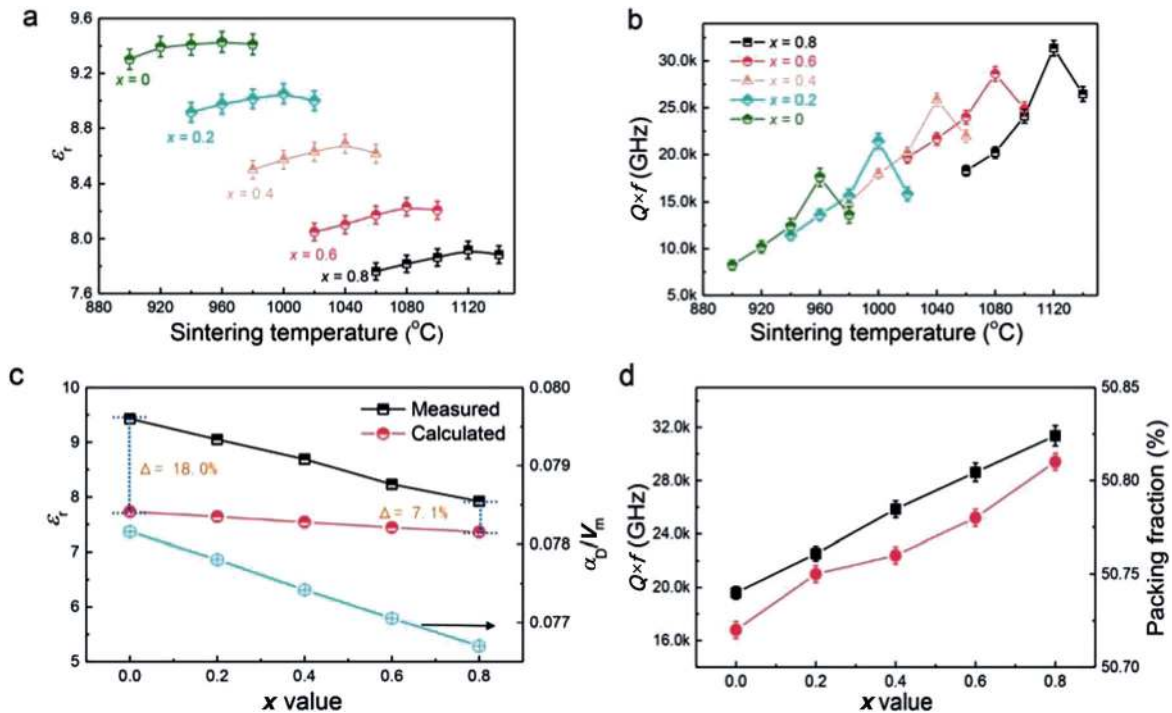
Fig. 10 Variations in the relative permittivity (ε_r) and quality factor ($Q{\times}f$) of Ba$_2$Cu$_{1-x}$Mg$_x$Ge$_2$O$_7$ (a, b) as a function of sintering temperature and (c, d) composition x value along with the change of the polarizability per unit volume (a_D^T / V_m) and packing fraction.

distribution. Thus, effects from these extrinsic factors (density, grain size, phase transition, second phase) on the dielectric properties can be ruled out. Hence, it is rational to conclude that the compositional variation in relative permittivity and quality factor is mainly controlled by the intrinsic influences.

Theoretically, the relative permittivity is inherently affected by the molecular polarizability (α_D^T) and unit volume (V_m) based on the Clausius–Mossotti equation $\varepsilon_\mathrm{r} = (1 + 2b\alpha_D^T / V_m) / (1 - b a_D^T / V_m)$ with $b = 4\pi/3$ as a constant, from which a direct correlation is accessible between ε_r and the polarizability per unit volume (a_D^T / V_m) [27]. Figure 10(c) shows the variation of a_D^T / V_m with composition, being characterized by a linear decrease. This result accounts for the underlying decrease of relative permittivity by magnesium substitution. Nevertheless, the calculated permittivities according to the Clausius–Mossotti equation are much smaller than the measured ones and the separation between them is about 7.1%–18.0%, decreasing with an increase of composition x, as shown in Fig. 10(c). Shannon ascribed such discrepancy as ionic or electronic conductivity, and/or structural distortion like rattling or compressed cations [27]. This large deviation, especially in Ba$_2$CuGe$_2$O$_7$, is an indicator of

the local structural distortion and Mg doping released such distortion, which would inevitably influence the physical properties, e.g., dielectric properties.

Such local distortion on relative permittivity can be reflected by the bond characteristics estimated by the electronegativity difference (Δe). According to Pauling' rule [28], the electronegativity difference for Ba$_2$Cu$_{1-x}$Mg$_x$Ge$_2$O$_7$ is calculated as

$$\Delta e = \frac{2\chi_{\mathrm{Ba-O}} + (1-x)\cdot\chi_{\mathrm{Cu-O}} + x\cdot\chi_{\mathrm{Mg-O}} + 2\chi_{\mathrm{Ge-O}}}{5}$$
$$= \frac{9.5 + 0.59x}{5} \tag{2}$$

Evidently, the electronegativity difference increases linearly with increasing x value, and the Δe are calculated as 1.900, 1.924, 1.947, 1.971, and 1.994 for $x = 0$, $x = 0.2$, $x = 0.4$, $x = 0.6$, and $x = 0.8$, respectively. The smaller Δe than 2 indicates the covalent bond feature which becomes more prominent with Mg content. The enhanced covalent bond should in principle dilute the polarizability (or permittivity) because of the more rigid structure. However, an opposite variation trend in the relative permittivity validates the existence of some rattling or compressed cations rooting in the local distortion with an increase

in Mg content.

The intrinsic influence on quality factor can be reflected by the packing fraction, as empirically summarized by Kim *et al.* [29,30]. For a certain material system, the higher of the packing fraction, the smaller space for the thermal motion of cations or anions, thus leading to lower dielectric losses [31]. The packing fraction is defined as the total volume of packed ions over the volume of the unit cell and the calculated values are shown in Fig. 10(d). A consistent increase in packing fraction with the quality factor is seen because magnesium substitution in BCG heightened the packing fraction, leading to more close packing of ions, which in turn results in low dielectric losses. On the other hand, the release of local structural distortion with Mg doping partly accounts for the diminished dielectric loss.

A linear increase in the temperature coefficient of resonance frequency (τ_f) is illustrated in Fig. 11 as the amount of Mg substitution increases from 0 to 0.8. It is well known that the τ_f value is correlated with the temperature coefficient of the relative permittivity (τ_ε) by the relation $\tau_f = -(\tau_\varepsilon/2 + \alpha_L)$ (α_L represents the linear thermal expansion coefficient, which is usually a constant about 10 ppm/℃). Thereby, the composition dependence of τ_f can be analyzed by studying the respective variation in τ_ε value. Derived from the definition for τ_ε, Bosman and Havinga divided the formula as follows [32]:

$$\tau_\varepsilon = \frac{1}{\varepsilon}\left(\frac{\partial \varepsilon}{\partial T}\right) = \frac{(\varepsilon-1)(\varepsilon+2)}{3\varepsilon}(A+B+C)$$

$$A = \frac{1}{\alpha_m}\left(\frac{\partial \alpha_m}{\partial T}\right)_V$$

$$B = \frac{1}{\alpha_m}\left(\frac{\partial \alpha_m}{\partial V}\right)_T\left(\frac{\partial V}{\partial T}\right)_P \qquad (3)$$

$$C = -\frac{1}{V}\left(\frac{\partial V}{\partial T}\right)_P$$

where ε and α_m represent the relative permittivity and polarizability, respectively. A is the direct dependence of the polarizability on temperature, being generally negative; B (generally positive) denotes the variation in polarizability concerning to the thermal change of volume; and C, in general negative, directly represents the volume change on temperature. The magnitudes of the variables B and C are similar and in opposing signs. Hence, the relative magnitude between A and ($B+C$) determines the signs and magnitude of τ_ε values.
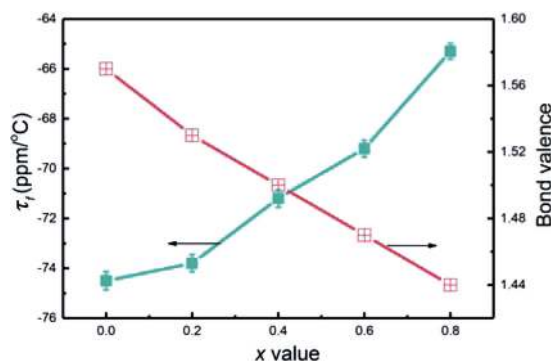

Fig. 11 Variations in the temperature coefficient of resonance frequency (τ_f) and the bond valence of Mg/Cu–O.

Particularly, both *B* and *C* terms involve in the volume variation, which would be reflected through the bond valence of ions. According to the previous reports on the calculation of bond valence [33–36], the Mg substitution effect on the bond valence of Cu–O in BCG is evaluated and shown in Fig. 11. In contrast to the variation tendency in the τ_f value, a steady decrease occurs in the bond valence. The decreasing bond valence reveals the reduced structural distortion caused by magnesium doping. The thermal energy is preferential to recover the structural distortion, giving rise to a larger ($B+C$) than A term, and thus a negative τ_f value. Therefore, the present rising τ_f value can be explained by the decrease in the structural distortion, as indicated by the decreased bond valence.

Table 2 compares the sintering temperature and microwave dielectric properties of some melilite structured ceramics. As expected, either Si-based or Ge-based melilite compounds possess low permittivities ($\varepsilon_r < 10$), moderate $Q \times f$ values, and negative τ_f values.

Table 2 Sintering temperature and microwave dielectric properties of some melilite structure ceramics

Ceramics	S.T. (℃)	Microwave properties		τ_f (ppm/℃)	Reference
		ε_r	$Q \times f$ (GHz)		
Ba$_2$ZnSi$_2$O$_7$	1200	8.09	26,634	−51.46	[9]
BaCo$_2$Si$_2$O$_7$	1060	9.26	31,135	−92.05	[10]
Ba$_2$MgGe$_2$O$_7$	1280	7.76	20,700	−55	[14]
Ba$_2$ZnGe$_2$O$_7$	1180	9.0	13,950	−75	[14]
Sr$_2$MgGe$_2$O$_7$	1330	8.56	28,800	−70.5	[15]
Sr$_2$ZnGe$_2$O$_7$	1290	8.51	35,700	−84.4	[15]
Sr$_2$CoSi$_2$O$_7$	1375	8.9	34,000	−56.7	[37]
Sr$_2$MnSi$_2$O$_7$	1375	8.8	32,000	−58.8	[37]
BaCu$_2$Si$_2$O$_7$	1025	8.29	46,085	−27.51	[38]
Ba$_2$CuGe$_2$O$_7$	960	9.43	20,000	−76	This work

Generally, Ba-containing compounds have relatively low sintering temperatures (~1200 ℃), while those Sr-containing counterparts have higher sintering temperatures (> 1300 ℃). What makes the present $Ba_2CuGe_2O_7$ unique is its lowest sintering temperature (960 ℃) amongst the listed melilites, which makes it a potential candidate for LTCC technology when using Ag as the inner electrode [39–41].

4   Conclusions

In summary, we fabricated a series of magnesium substituted $Ba_2CuGe_2O_7$ ceramics and detailed the effects of magnesium on the sintering behavior, structure (both macroscopic and microscopic), and microwave dielectric properties. XRD and SEM results revealed that magnesium doping induced limited variations in the macroscopic structure and microstructure features. On the contrary, the densification temperature was remarkably raised from 960 to 1120 ℃; meanwhile, Raman spectra provided an indicator of considerable change in the local structure, as characterized by the alteration in the Raman shift and width. Moreover, on increasing the magnesium content, the dielectric properties decreased from 9.43 to 7.92 which are attributed to the lower ionic polarizability of magnesium and the released local structural distortion, while the quality factory ($Q \times f$) increased from 19,560 to 31,370 GHz because of the increasing packing fraction. A monotonous increase in τ_f was induced by magnesium substitution, which was explained by the decreased bond valence of Cu/Mg–O. This work provides a potential method to tune the thermal stability of Ba_2CuGeO_7 realized by increasing the bond strength through substituting larger cations, e.g., Ni^{2+} for Cu^{2+} or Si^{4+} for Ge^{4+}.

Acknowledgements

References

[1] Sebastian T. *Dielectric Materials for Wireless Communications*. Oxford, UK: Elseiver Publishers. 2008.

[2] Wu MJ, Zhang YC, Xiang MQ. Synthesis, characterization and dielectric properties of a novel temperature stable $(1-x)CoTiNb_2O_8-xZnNb_2O_6$ ceramic. *J Adv Ceram* 2019, **8**: 228–237.

[3] Li CC, Xiang HC, Xu MY, et al. Li_2AGeO_4 (A = Zn, Mg): Two novel low-permittivity microwave dielectric ceramics with olivine structure. *J Eur Ceram Soc* 2018, **38**: 1524–1528.

[4] Lin QB, Song KX, Liu B, et al. Vibrational spectroscopy and microwave dielectric properties of $AY_2Si_3O_{10}$ (A = Sr, Ba) ceramics for 5G applications. *Ceram Int* 2020, **46**: 1171–1177.

[5] Zhou D, Pang LX, Wang DW, et al. High permittivity and low loss microwave dielectric suitable for 5G resonators and low temperature co-fired ceramic architecture. *J Mater Chem C* 2017, **5**: 10094–10098.

[6] Ullah A, Liu HX, Hao H, et al. Influence of TiO_2 additive on sintering temperature and microwave dielectric properties of $Mg_{0.90}Ni_{0.1}SiO_3$ ceramics. *J Eur Ceram Soc* 2017, **37**: 3045–3049.

[7] Song ME, Kim JS, Joung MR, et al. Synthesis and microwave dielectric properties of $MgSiO_3$ ceramics. *J Am Ceram Soc* 2008, **91**: 2747–2750.

[8] Nguyen NH, Lim JB, Nahm S, et al. Effect of Zn/Si ratio on the microstructural and microwave dielectric properties of Zn_2SiO_4 ceramics. *J Am Ceram Soc* 2007, **90**: 3127–3130.

[9] Zou ZY, Lan XK, Lu WZ, et al. Novel high Curie temperature $Ba_2ZnSi_2O_7$ ferroelectrics with low-permittivity microwave dielectric properties. *Ceram Int* 2016, **42**: 16387–16391.

[10] Song XQ, Lei W, Xie MQ, et al. Sintering behaviour, lattice energy and microwave dielectric properties of melilite-type $BaCo_2Si_2O_7$ ceramics. *Mater Res Express* 2020, **6**: 126322.

[11] Zou ZY, Chen ZH, Lan XK, et al. Weak ferroelectricity and low-permittivity microwave dielectric properties of $Ba_2Zn_{(1+x)}Si_2O_{(7+x)}$ ceramics. *J Eur Ceram Soc* 2017, **37**: 3065–3071.

[12] Hanuza J, Mączka M, Ptak M, et al. Polarized IR and Raman spectra, temperature dependence of phonons and lattice dynamic calculations for $M'_2M''Ge_2O_7$ pyrogermanates (M′ = Sr, Ba; M″ = Mg, Zn). *J Raman Spectrosc* 2011, **42**: 782–789.

[13] Sazonov A, Hutanu V, Meven M, et al. Crystal structure of magnetoelectric $Ba_2MnGe_2O_7$ at room and low temperatures by neutron diffraction. *Inorg Chem* 2018, **57**: 5089–5095.

[14] Li CC, Yin CZ, Chen JQ, et al. Crystal structure and dielectric properties of germanate melilites $Ba_2MGe_2O_7$ (M = Mg and Zn) with low permittivity. *J Eur Ceram Soc* 2018, **38**: 5246–5251.

[15] Yin CZ, Tang Y, Chen JQ, et al. Two low-permittivity melilite ceramics in the SrO–MO–GeO_2 (M = Mg, Zn) system and their temperature stability through compositional modifications. *J Eur Ceram Soc* 2020, **40**: 1186–1190.

[16] Lai YM, Su H, Wang G, *et al*. Improved microwave dielectric properties of CaMgSi$_2$O$_6$ ceramics through CuO doping. *J Alloys Compd* 2019, **772**: 40–48.

[17] Pang LX, Zhou D. Microwave dielectric properties of low-firing Li$_2$MO$_3$ (M = Ti, Zr, Sn) ceramics with B$_2$O$_3$–CuO addition. *J Am Ceram Soc* 2010, **93**: 3614– 3617.

[18] Lai YM, Tang XL, Huang X, *et al*. Phase composition, crystal structure and microwave dielectric properties of Mg$_{2-x}$Cu$_x$SiO$_4$ ceramics. *J Eur Ceram Soc* 2018, **38**: 1508–1516.

[19] Wang G, Zhang DN, Xu F, *et al*. Correlation between crystal structure and modified microwave dielectric characteristics of Cu^{2+} substituted Li$_3$Mg$_2$NbO$_6$ ceramics. *Ceram Int* 2019, **45**: 10170–10175.

[20] Kim ES, Chun BS, Yoon KH. Dielectric properties of [Ca$_{1-x}$(Li$_{1/2}$Nd$_{1/2}$)$_x$]$_{1-y}$Zn$_y$TiO$_3$ ceramics at microwave frequencies. *Mat Sci Eng B* 2003, **99**: 93–97.

[21] Yin CZ, Xiang HC, Li CC, *et al*. Low-temperature sintering and thermal stability of Li$_2$GeO$_3$-based microwave dielectric ceramics with low permittivity. *J Am Ceram Soc* 2018, **101**: 4608–4614.

[22] Kim WS, Kim ES, Yoon KH. Effects of Sm^{3+} substitution on dielectric properties of Ca$_{1-x}$Sm$_{2x/3}$TiO$_3$ ceramics at microwave frequencies. *J Am Ceram Soc* 2004, **82**: 2111–2115.

[23] Shi F, Dong HL. Vibrational modes and structural characteristics of (Ba$_{(0.3)}$Sr$_{(0.7)}$)[(Zn$_{(x)}$Mg$_{(1-x)}$)$_{(1/3)}$Nb$_{(2/3)}$]O$_3$ solid solutions. *Dalton Trans* 2011, **40**: 11591–11598.

[24] Manan A, Ullah Z, Ahmad AS, *et al*. Phase microstructure evaluation and microwave dielectric properties of (1–*x*)Mg$_{0.95}$Ni$_{0.05}$Ti$_{0.98}$Zr$_{0.02}$O$_3$–*x*Ca$_{0.6}$La$_{0.8/3}$TiO$_3$ ceramics. *J Adv Ceram* 2018, **7**: 72–78.

[25] Song XQ, Lu WZ, Wang XC, *et al*. Sintering behaviour and microwave dielectric properties of BaAl$_{2-2x}$(ZnSi)$_x$Si$_2$O$_8$ ceramics. *J Eur Ceram Soc* 2018, **38**: 1529–1534.

[26] Pan HL, Cheng L, Wu HT. Relationships between crystal structure and microwave dielectric properties of Li$_2$(Mg$_{1-x}$Co$_x$)$_3$TiO$_6$ (0 ⩽ *x* ⩽ 0.4) ceramics. *Ceram Int* 2017, **43**: 15018–15026.

[27] Shannon RD. Dielectric polarizabilities of ions in oxides and fluorides. *J Appl Phys* 1993, **73**: 348–366.

[28] Allred AL. Electronegativity values from thermochemical data. *J Inorg Nucl Chem* 1961, **17**: 215–221.

[29] Kim ES, Chun BS, Freer R, *et al*. Effects of packing fraction and bond valence on microwave dielectric properties of A^{2+}B^{6+}O$_4$ (A^{2+}: Ca, Pb, Ba; B^{6+}: Mo, W) ceramics. *J Eur Ceram Soc* 2010, **30**: 1731–1736.

[30] Liao QW, Li LX, Ren X, *et al*. New low-loss microwave dielectric material ZnTiNb$_2$O$_8$. *J Am Ceram Soc* 2011, **94**: 3237–3240.

[31] Xiao M, Gu QQ, Zhou ZQ, *et al*. Study of the microwave dielectric properties of (La$_{1-x}$Sm$_x$)NbO$_4$ (*x* = 0–0.10) ceramics via bond valence and packing fraction. *J Am Ceram Soc* 2017, **100**: 3952–3960.

[32] Pan HL, Cheng L, Wu HT. Relationships between crystal structure and microwave dielectric properties of Li$_2$(Mg$_{1-x}$Co$_x$)$_3$TiO$_6$ (0 ⩽ *x* ⩽ 0.4) ceramics. *Ceram Int* 2017, **43**: 15018–15026.

[33] Park HS, Yoon KH, Kim ES. Relationship between the bond valence and the temperature coefficient of the resonant frequency in the complex perovskite (Pb$_{1-x}$Ca$_x$)[Fe$_{0.5}$(Nb$_{1-y}$Ta$_y$)$_{0.5}$]O$_3$. *J Am Ceram Soc* 2001, **84**: 99–103.

[34] Brese NE, O'Keeffe M. Bond-valence parameters for solids. *Acta Cryst* 1991, **B47**: 192–197.

[35] Brown ID, Altermatt D. Bond-valence parameters obtained from a systematic analysis of the Inorganic Crystal Structure Database. *Acta Cryst* 1985, **B41**: 244–247.

[36] Kim ES, Kim SH. Effects of structural characteristics on microwave dielectric properties of (1–*x*)CaWO$_4$–*x*LaNbO$_4$ ceramics. *J Electroceram* 2006, **17**: 471–477.

[37] Joseph T, Sebastian MT. Microwave dielectric properties of (Sr$_{1-x}$A$_x$)$_2$(Zn$_{1-x}$B$_x$)Si$_2$O$_7$ ceramics (A = Ca, Ba and B = Co, Mg, Mn, Ni). *J Am Ceram Soc* 2010, **93**: 147–154.

[38] Song XQ, Zou ZY, Lu WZ, *et al*. Crystal structure, lattice energy and microwave dielectric properties of melilite-type Ba$_{1-x}$Sr$_x$Cu$_2$Si$_2$O$_7$ solid solutions. *J Alloys Compd* 2020, **835**: 155340.

[39] Hsiang HI, Chen CC, Yang SY. Microwave dielectric properties of Ca$_{0.7}$Nd$_{0.2}$TiO$_3$ ceramic-filled CaO–B$_2$O$_3$–SiO$_2$ glass for LTCC applications. *J Adv Ceram* 2019, **8**: 345–351.

[40] Zhou J. Towards rational design of low-temperature co-fired ceramic (LTCC) materials. *J Adv Ceram* 2012, **1**: 89–99.